Journal of Alloys and Compounds 527 (2012) 30–35

Contents lists available at SciVerse ScienceDirect

Journal of Alloys and Compounds

journal homepage: www.elsevier.com/locate/jallcom

Synthesis and photocatalytic activity of TiO_2@CdS and CdS@TiO_2 double-shelled hollow spheres

H.L. Meng[a], C. Cui[a,*], H.L. Shen[a], D.Y. Liang[a], Y.Z. Xue[a], P.G. Li[a], W.H. Tang[a,b]

[a] Center for Optoelectronics Materials and Devices, Department of Physics, Zhejiang Sci-Tech University, Hangzhou 310018, China
[b] State Key Laboratory of Information Photonics & Optical Communication, School of Science, Beijing University Posts and Telecommunications, Beijing 100876, China

ARTICLE INFO

Article history:
Received 30 December 2011
Received in revised form 28 January 2012
Accepted 5 February 2012
Available online xxx

Keywords:
TiO_2
Double-shelled hollow spheres
Photocatalysis

ABSTRACT

Double-shelled TiO_2@CdS and CdS@TiO_2 hollow spheres with diameter about 540 nm have been successfully synthesized using SiO_2 nanospheres as sacrificial templates. The double-shelled hollow spheres (DHS) structure consists of a 50 nm-thick TiO_2 shell and a 20 nm-thick CdS shell, which are, respectively, formed with TiO_2 and CdS nanocrystals. The TiO_2@CdS and CdS@TiO_2 DHS possess large specific surface area (138.3 $m^2 g^{-1}$ and 102.4 $m^2 g^{-1}$) and very narrow pore size distribution (3–7 nm). The UV–vis spectra of the TiO_2@CdS and CdS@TiO_2 DHS exhibit strong absorption in visible light region and the absorption edges of the two DHS samples are around 515 nm and 540 nm, corresponding to bandgap energy of 2.4 eV and 2.3 eV. The photocatalytic properties of the two DHS samples, pure TiO_2 and CdS hollow spheres on degradation of rhodamine B (RhB) solution were studied, and the results indicated that TiO_2@CdS DHS performed the best photocatalytic activity among them. The mechanism of photocatalysis occurred on the two CdS coupled TiO_2 DHS under visible light is discussed.

1. Introduction

TiO_2, with a bandgap of 3.2 eV, has been used as a popular photocatalytic material, because of its superior photocatalytic activity, biological and chemical inertness, low cost, long-term stability and nontoxicity [1,2]. TiO_2 absorbs wavelength only in the ultraviolet region, which great limits the efficient utilization of solar energy conversation [3–5]. A variety of ways have been pursued to extend the response of photocatalysts into visible-light region. These include doping TiO_2 with metallic (Ag, Pt, Cr, Fe) and nonmetallic (B, C, N) elements or combining TiO_2 with some narrow-bandgap semiconductors (CdS, CdSe, WO_3, and Bi_2WO_6) or polymeric semiconductors [6–12]. Among the above methods, coupling TiO_2 with a narrower bandgap semiconductor with a higher conduction band (CB) than that of TiO_2 has been proved to be an effective approach to accommodate the visible-light photon energy. In such semiconductor heterostructures, photo-generated electrons transfer from the CB of the narrower-bandgap semiconductor to that of TiO_2, which suppress the recombination of photo-generated electron–hole pairs [11–16]. CdS, one of the most important II–VI group semiconductors with bandgap of 2.4 eV (cubic phase), has been widely used in TiO_2/CdS coupled heterojunction to improve the photo-electron conversion efficiency of photocatalysis and solar cell [13–16].

In the past years, there were many reports on TiO_2 hollow micro-/nanostructures, such structures have been demonstrated potential applications in photocatalysis and solar cell for their properties of low density, high surface area, and large light-harvesting efficiency [17–22]. Kondo et al. prepared submicron-scale anatase TiO_2 hollow spheres using a template method and found that the hollow spheres enhanced performance of TiO_2 in photocatalysis and dye sensitized solar cell (DSSC), and they ascribed such enhancement to the specific diffraction and/or reflection of the illuminated lights on the TiO_2 hollow spheres [23]. Wang et al. found that size-tailored TiO_2 hollow spheres can tune light scattering in a wide visible-light range. They successfully achieved a notable 10% improvement of solar-to-electric conversion efficiency by introducing the TiO_2 hollow sphere scattering layer in quantum dot-sensitized solar cells [24]. However, few studies have been reported on the TiO_2 hollow sphere coupled with narrower-bandgap semiconductors.

In this paper, we designed two novel TiO_2/CdS DHS heterostructures, which are of particular interest because they may combine the advantages of hollow spheres with the advantages of TiO_2/CdS heterojunction. The DHS heterostructures are named as TiO_2@CdS and CdS@TiO2. The former represents a TiO_2 inner shell covered with a CdS outer shell, and the later represents a CdS inner shell covered with a TiO_2 shell. The DHS structures were synthesized using SiO_2 nanospheres as sacrificial templates. The morphology,

* Corresponding author. Tel.: +86 571 8684 3468.
E-mail address: cancui@zstu.edu.cn (C. Cui).

0925-8388/$ – see front matter © 2012 Elsevier B.V. All rights reserved.
doi:10.1016/j.jallcom.2012.02.043

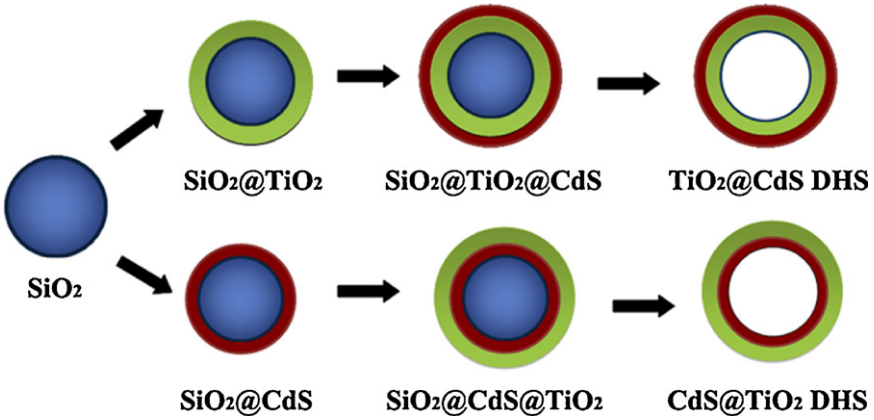

Fig. 1. Schematic diagram of the synthesis procedure of the double-shell hollow spheres (DHS).

crystal structure, optical properties and photocatalytic behaviors of the DHS were investigated systematically. Both TiO_2@CdS and CdS@TiO_2 DHS are well homogeneous and exhibit wide-absorption response in the visible-light region. Their photocatalytic degradations of RhB under visible-light illumination were investigated comparatively, indicating that the photocatalytic activity of TiO_2@CdS DHS is better than that of CdS@TiO_2 DHS.

2. Experimental and characterization

2.1. Synthesis of TiO_2@CdS and CdS@TiO_2 DHS

The schematic diagram for the synthesis of TiO_2@CdS and CdS@TiO_2 DHS is shown in Fig. 1. Firstly, SiO_2 nanosphere templates were synthesized by a modified Stöber method [25]. Then, the SiO_2 nanosphere were covered with TiO_2 (or CdS) and CdS (or TiO_2) in sequence to form SiO_2@TiO_2@CdS (or SiO_2@CdS@TiO_2) core–shell spheres. Finally, the SiO_2 cores were removed from the obtained core–shell spheres by using hydrothermal treatment in NaOH solution. Single shelled TiO_2 hollow spheres and CdS hollow spheres were also synthesized to be taken as reference. The detailed synthesis procedure was described as follows.

2.1.1. Synthesis of SiO_2 nanospheres

SiO_2 nanospheres were synthesized by the catalytic hydrolysis of tetraethoxysilane (TEOS) at 40 °C using aqueous ammonia as catalyst. 5 mL of TEOS was dissolved in 45 mL of ethanol to obtain solution A; 5 mL of aqueous ammonia and 10 mL of deionized water were dissolved in 35 mL of ethanol to obtain solution B. Then, solution A was added to solution B, vigorously stirred at 40 °C for 2.5 h. The solid was centrifuged and washed three times with ethanol. The average diameter of the SiO_2 nanospheres was around 400 nm.

2.1.2. Synthesis of SiO_2@TiO_2 core–shell spheres

0.3 g prepared SiO_2 nanospheres were ultrasonic dispersed in 100 mL of ethanol to obtain solution A. 2 mL of tetrabutyl titanate (TBT) was dissolved in 100 mL of ethanol to obtain solution B. Solution B and 1.5 mL of aqueous ammonia were added to solution A, vigorously stirred at 60 °C for 3 h. The solid SiO_2@TiO_2 core–shell spheres were centrifuged and carefully washed with ethanol and dried in air. Then, they were annealed at 550 °C for 1 h in air to crystallize TiO_2.

2.1.3. Synthesis of SiO_2@TiO_2@CdS core–shell spheres

CdS shells of SiO_2@TiO_2@CdS core–shell spheres were fabricated by an ultrasound-driven method. In a typical synthesis, 0.6 g SiO_2@TiO_2 core–shell spheres templates were ultrasonic dispersed in 300 mL of deionized water. 15 mL of 0.1 M $CdCl_2$ solution, 20 mL of 0.1 M sodium citrate solution and 30 mL of 0.1 M thiourea solution were prepared. These four kinds of solution were mixed, and the pH value was modulated to ~10.50 by dropping a certain amount of ammonia solution. The reaction was accomplished under continuously sonication at 65 °C for 1.5 h. Then, the solid SiO_2@TiO_2@CdS core–shell spheres were centrifuged and carefully washed with deionized water.

2.1.4. Synthesis of SiO_2@CdS core–shell spheres

CdS shells of SiO_2@CdS core–shell spheres were prepared according to a process described in Section 2.1.3 with minor modification, using 0.3 g SiO_2 nanospheres as templates.

2.1.5. Synthesis of SiO_2@CdS@TiO_2 core–shell spheres

TiO_2 shells of SiO_2@CdS@TiO_2 core–shell spheres were prepared according to a process described in Section 2.1.2 with minor modification, using 0.5 g SiO_2@CdS core–shell spheres as templates. Then, the obtained SiO_2@CdS@TiO_2 core–shell spheres were annealed at 550 °C for 1 h in N_2 atmosphere to crystallize TiO_2.

2.1.6. Synthesis of TiO_2@CdS or CdS@TiO_2 DHS

SiO_2@TiO_2@CdS or SiO_2@CdS@TiO_2 core–shell spheres were placed in the 50 mL Teflon-lined autoclave with a stainless steel tank and then the autoclave was filled to 80% capacity with 1 mol/L NaOH. After completely mixing, the autoclave was sealed and placed in a furnace heating at 80 °C for 4 h. The autoclave was then naturally cooled to room temperature with furnace. Finally, the product was collected by centrifugation and washed several times with distilled water.

2.2. Photocatalytic activity test

Photocatalytic activity of the samples was evaluated by degradation of RhB under the illumination of a 500 W Xe lamp with a 400 nm cutoff filter. 0.05 g of photocatalyst was added into 50 mL of RhB solution (2×10^{-5} mol/L) and stirred in dark for 30 min before illumination to ensure the establishment of an adsorption–desorption equilibrium between the photocatalyst and RhB. The temperature of suspension was maintained at 25 °C by circulation of water through an external cooling coil during the process. Oxygen under atmospheric pressure was bubbled through the reaction continuously. At 20 min intervals, the absorption spectrum of a 3 mL of solution was recorded on a UV–vis spectrophotometer.

2.3. Catalyst characterization

X-ray powder diffraction (XRD) measurement was carried out in a Bruker D8 Advance X-ray diffractometer using Cu Kα (λ = 1.5406 Å) radiation at 40 kV and 40 mA. Scanning electron microscopy (SEM) images were taken on a Hitachi S-4800 field emission scanning electron microscope. Transmission electron microscopy (TEM) images and selected-area electron diffraction (SAED) images were recorded on a JEM-2100 microscope (200 kV). The nitrogen adsorption–desorption isotherms were obtained at 77 K with a Micromeritics ASAP 2020 micropore analysis system. The specific surface areas were determined using the Barrett–Emmett–Teller (BET) method, and the average pore diameters were calculated using the Barrett–Joyner–Halenda (BJH) method. UV–vis diffuse reflectance spectra (UV–vis DRS) were measured using a Perkin Elmer Lambda 900 UV–vis spectrophotometer. UV–vis absorption spectra analysis of the RhB solution was performed on a Varian Cary 50 spectrophotometer.

3. Results and discussion

Fig. 2 shows the SEM images of the intermediate products obtained at different synthesis steps. The samples remain spherical during the synthesis procedure. The average diameters of SiO_2@TiO_2, SiO_2@TiO_2@CdS, SiO_2@CdS and SiO_2@CdS@TiO_2 core–shell spheres are around 500 nm, 540 nm, 440 nm, 540 nm, respectively, indicating that the thicknesses of the CdS and TiO_2 shells are around 20 nm and 50 nm, respectively. The broken spheres in Fig. 2c and f demonstrate the formation of hollow spheres. It is also noted that the surface of the TiO_2@CdS DHS is rougher than that of the CdS@TiO_2 DHS. The rough CdS shell is formed via the formation of CdS nanoflakes during the hydrothermal treatment in NaOH solution.

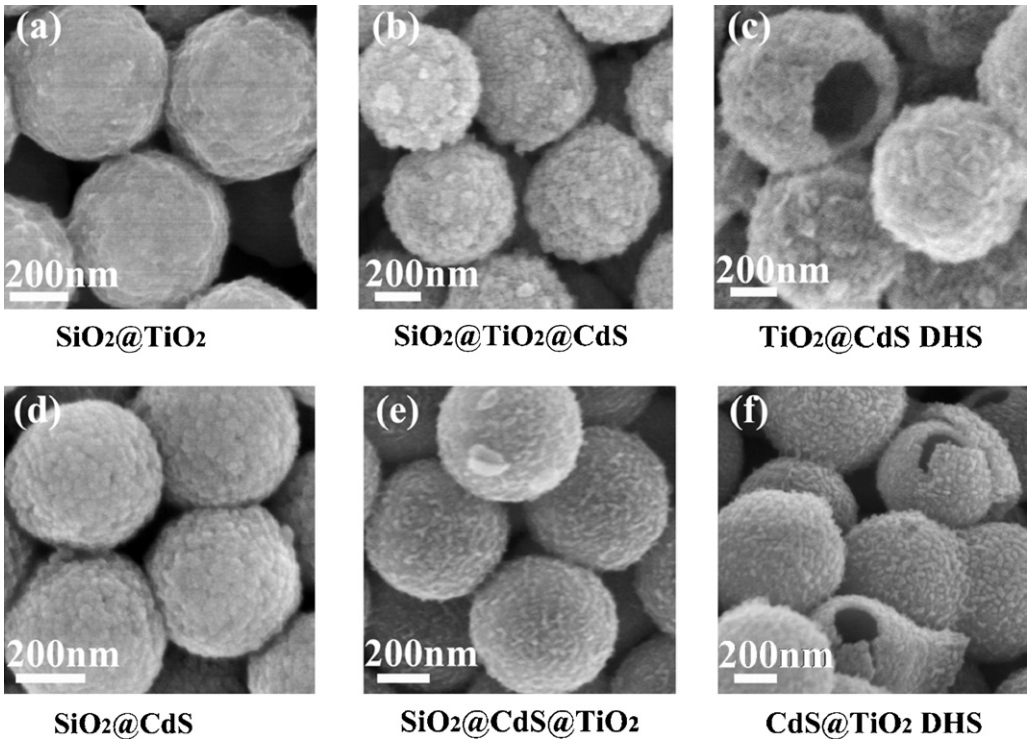

Fig. 2. SEM images of the intermediate products obtained at different synthesis steps in Fig. 1.

Fig. 3 shows the XRD patterns of TiO_2@CdS and CdS@TiO_2 DHS samples. In Fig. 3a, the diffraction peaks can be indexed to anatase TiO_2 (JCPDS card No. 21-1272) and cubic phase CdS (JCPDS card No. 65-2887), indicating that both TiO_2 and CdS phases in TiO_2@CdS DHS are well-crystallized. The broad diffraction peaks imply that the crystalline grains are on nanoscale. The average grain size is evaluated according to the Scherrer equation using the full width at half maximum (FWHM) of the diffraction peaks. The average size of the anatase TiO_2 and cubic phase CdS nanocrystals in TiO_2@CdS DHS sample are about 13 nm and 7 nm, respectively [26]. In Fig. 3b, beside the diffraction peaks of anatase TiO_2 and cubic phase CdS, diffraction peaks of hexagonal phase CdS (JCPDS card No. 65-3414) are also observed, indicating that another CdS phase exists in the CdS@TiO_2 DHS sample. The average sizes of anatase TiO_2, cubic phase CdS and hexagonal phase CdS nanocrystals in the CdS@TiO_2 DHS are about 19 nm, 14 nm and 17 nm. The relatively larger crystallite size and formation of hexagonal phase CdS in CdS@TiO_2 DHS sample are ascribed to the thermal treatment at 550 °C, which is used to crystallize anatase TiO_2.

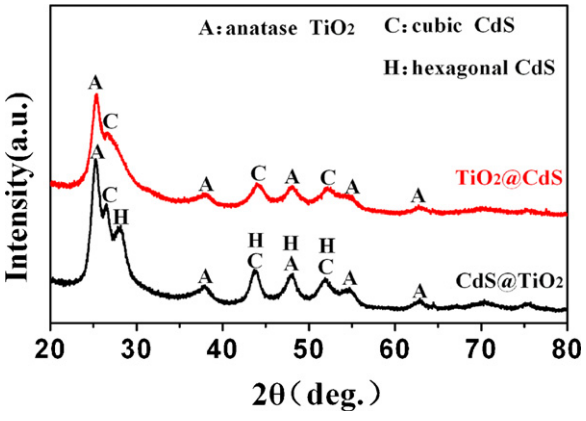

Fig. 3. XRD patterns of TiO_2@CdS DHS and CdS@TiO_2 DHS.

The TEM images of TiO_2@CdS and CdS@TiO_2 DHS are shown in Fig. 4. In Fig. 4a and b, the color contrast between the central and fringe region of the spheres confirms the formation of hollow spherical structures with shells of about 70 nm in thickness. The TEM image of CdS@TiO_2 DHS (Fig. 4b) displays a well-defined double-shelled structure due to the color contrast of CdS and TiO_2 shells. Whereas, as shown in Fig. 4a, the outer CdS shell in TiO_2@CdS DHS is formed with rough CdS nanoflakes, which results in low color contrast of CdS and TiO_2 in the TEM image. High resolution transmission electron microscopy (HRTEM) images in Fig. 4c and d also reveal the formation of highly crystallized nanocrystals with random orientation. The clear fringes in the HRTEM images allow for the identification of the crystallographic spacing of TiO_2 and CdS nanocrystals. The lattice fringes of 0.337 nm, 0.356 nm and 0.351 nm are corresponding to the (1 1 1) crystal plane of cubic CdS phase, the (1 0 0) plane of hexagonal CdS phase and (1 0 1) plane of anatase TiO_2, respectively. The close contact between CdS and TiO_2 nanocrystals in the HRTEM images reveals the existence of CdS/TiO_2 heterojunction in the interfacial area of the two shells. The SAED pattern shows several Debye–Scherrer rings (insets in Fig. 4c and d), corresponding to the reflections of TiO_2 and CdS nanocrystals.

Fig. 5 shows pore size distribution curves calculated from the nitrogen adsorption–desorption isotherms by Barrett–Joyner–Halenda (BJH) method and the corresponding isotherms (inset) for the TiO_2@CdS and CdS@TiO_2 DHS samples. Both samples exhibit a type IV isotherm with a type H3 hysteresis loop, indicating the pore-size distribution profiles are in microporous region [27]. The specific surface area of the TiO_2@CdS DHS is 138.3 $m^2\,g^{-1}$. The pore diameter of the TiO_2@CdS DHS is 6.19 nm (estimated using the desorption branch of the isotherm). In comparison with TiO_2@CdS DHS, CdS@TiO_2 DHS has a smaller average pore diameter (4.05 nm) and a smaller specific surface area (102.4 $m^2\,g^{-1}$), which are ascribed to the formation of relatively

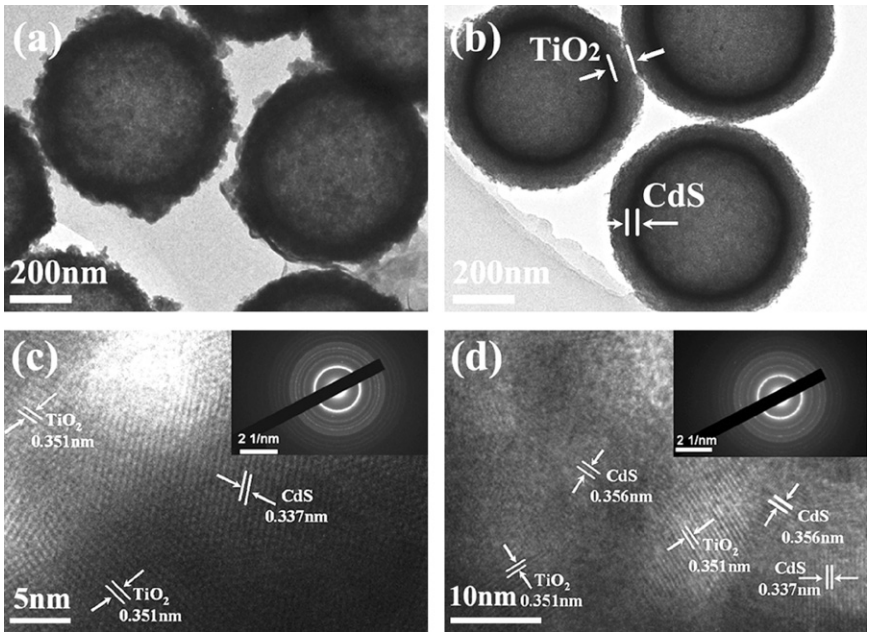

Fig. 4. (a) TEM image of TiO_2@CdS DHS, (b) TEM image of CdS@TiO_2 DHS, (c) HRTEM image and SAED pattern (inset) of TiO_2@CdS DHS, and (d) HRTEM and SAED (inset) images of CdS@TiO_2 DHS.

large-sized TiO_2 nanocrystals during the subsequent annealing at 550 °C.

The UV–vis DRS spectra were measured to investigate the optical absorption property of the DHS samples. Pure cubic CdS hollow spheres and anatase TiO_2 hollow spheres synthesized with the template method were also studied for comparison. The absorption onsets are determined by linear extrapolation from the inflection point of the curve to the baseline. As shown in Fig. 6, the absorption onsets for pure CdS and TiO_2 hollow spheres are around 390 nm and 510 nm, corresponding to bandgap energy of 3.2 eV and 2.4 eV. Compared to anatase TiO_2 hollow spheres, the absorption onsets of the CdS coupled TiO_2 DHS samples red shift to longer wavelength within the range of visible light. As a result, the sample color was changes from white (anatase TiO_2) to lemon for TiO_2@CdS DHS and chrysoidine for CdS@TiO_2 DHS, as shown in the insets of Fig. 6. The absorption onsets of TiO_2@CdS and CdS@TiO_2 DHS are around 515 nm and 540 nm, which are very close to the absorption onsets of pure CdS hollow spheres and they are corresponding to bandgap energies of 2.4 eV and 2.3 eV, respectively. Since the TiO_2 nanocrystal has a bandgap above 3.2 eV, the bandgap of CdS coupled TiO_2 DHS is primarily determined by the CdS shell. There are two reasons leaded to the different bandgap of the DHS samples. The first reason is the different size of CdS nanocrystals in the two DHS samples. The average size of the CdS nanocrystal in TiO_2@CdS DHS is about 7 nm, which is smaller than that in CdS@TiO_2 DHS (14 nm for cubic phase and 17 nm for hexagonal phase CdS nanocrystals). Smaller size of the CdS nanocrytals result in a slightly larger bandgap of TiO_2@CdS DHS. The second reason is the existence of hexagonal phase CdS in CdS@TiO_2 DHS. The bandgap of hexagonal phase CdS (2.3 eV) is smaller than that of cubic phase CdS (2.4 eV),

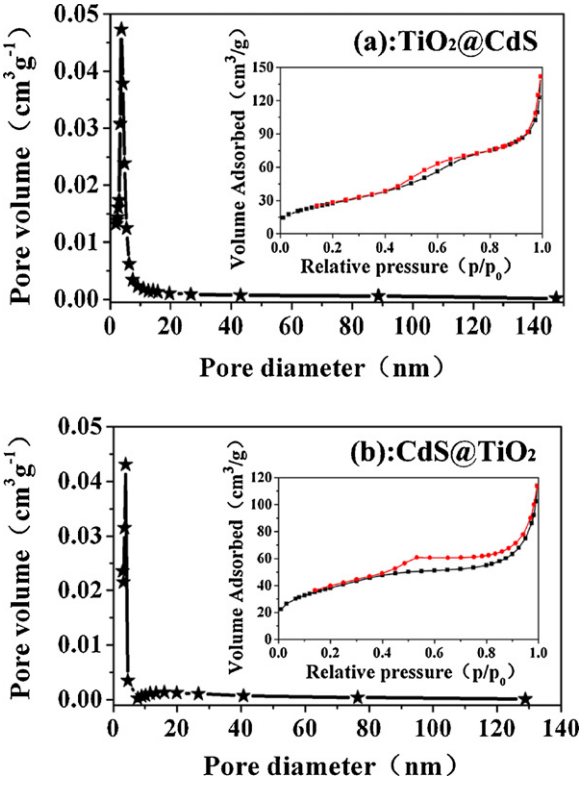

Fig. 5. BET/BJH analyses of (a) TiO_2@CdS DHS and (b) CdS@TiO_2 DHS.

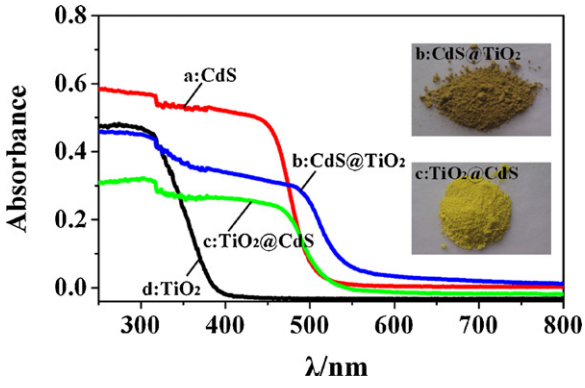

Fig. 6. UV–vis DRS spectra of (a) CdS hollow spheres, (b) CdS@TiO_2 DHS, (c) TiO_2@CdS DHS, and (d) TiO_2 hollow spheres.

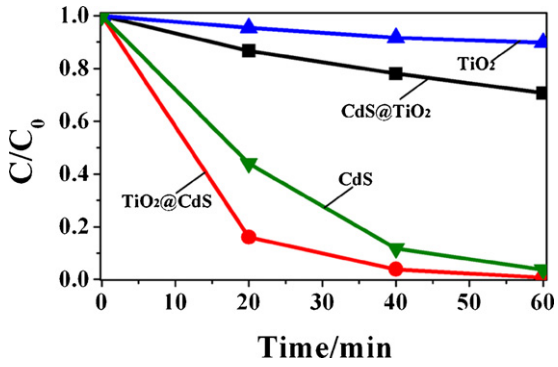

Fig. 7. RhB reduction as a function of illumination time for TiO_2 hollow spheres, CdS hollow spheres, CdS@TiO_2 DHS, and TiO_2@CdS DHS.

thus the hexagonal phase CdS lead to smaller bandgap of CdS@TiO_2 DHS.

The photocatalytic activity of TiO_2@CdS and CdS@TiO_2 DHS was evaluated by degradation of RhB dye in water under visible light illumination ($\lambda > 400$ nm). The pure TiO_2 hollow spheres and CdS hollow spheres were studied as reference. Fig. 7 shows the photocatalytic degradation curves of RhB as a function of time. The first-order linear relationship is revealed by the plots of C/C_0 vs illumination time, where C is the concentration of RhB at the illumination time t and the C_0 is the initial concentration. As we can see, the degradation of RhB by the pure TiO_2 hollow spheres is not significant and only about 5% of RhB was degraded in 60 min. The CdS@TiO_2 DHS shows an intergraded photocatalytic activity among the four samples and about 20% of RhB was degraded in 60 min. The TiO_2@CdS DHS and pure CdS hollow spheres samples demonstrate the highest visible-light photocatalytic activity, nearly 100% RhB was degraded in 60 min. However, the TiO_2@CdS DHS exhibits a faster degradation rate at the early stage of the photocatalysis process. These experiment results indicate that the CdS/TiO_2 coupling shows enhancement on the degradation of RhB, whereas the two kinds of DHS have quite different photocatalytic activity due to their different architecture structures.

The enhancement of the photocatalytic activity in the CdS coupled TiO_2 system is attributed to the interaction between CdS and TiO_2. By coupling of CdS with TiO_2, internal field is established between two semiconductors, and it promotes the photo-generated electrons and holes migrate to different field direction. Since the CB of CdS is higher by 0.5 eV than that of TiO_2, the electrons in the valence band (VB) of CdS are excited to its CB and then quickly transfer into the CB of TiO_2 under visible light illumination [4]. Thus, an efficient charge separation is achieved (Eqs. (1) and (2)). When oxygen is present, it can be reduced to superoxide radical anion ($O_2^{\bullet -}$) or hydrogen peroxide (H_2O_2) by the photo-generated electrons on the surface of TiO_2 (Eqs. (3) and (4)). These new formed intermediates can interreact to form hydroxyl radical ($OH^\bullet$) (Eq. (5)). Then, RhB molecules are decomposed by hydroxyl radicals through an oxidation process (Eq. (6)) [27]. The valence band holes in CdS plays another important role in the degradation of RhB. Although the holes in CdS theoretically cannot react with hydroxyl groups (or H_2O) to produce $OH^\bullet$ radicals, because the valence band potential (+1.4 eV) of CdS is more cathodic than the redox potential of $^\bullet OH/H_2O$ (+2.27 eV), they can degrade RhB directly (Eq. (7)) [4,28].

$$(TiO_2/CdS) + h\upsilon \rightarrow TiO_2/CdS(e^- + h^+) \quad (1)$$

$$TiO_2/CdS(e^- + h^+) \rightarrow TiO_2(e^-)/CdS(h^+) \quad (2)$$

$$(e^-) + O_2 \rightarrow O_2^{\bullet -} \quad (3)$$

$$O_2 + 2e^- + 2H^+ \rightarrow H_2O_2 \quad (4)$$

$$H_2O_2 + O_2^{\bullet -} \rightarrow OH^\bullet + OH^- + O_2 \quad (5)$$

$$OH^\bullet + RhB \rightarrow \text{degraded or mineralized products} \quad (6)$$

$$CdS(h^+) + RhB \rightarrow \text{degraded or mineralized products} \quad (7)$$

Because of the sensitization of the CdS inner shell, CdS@TiO_2 DHS displays a better photocatalytic activity than pure anatase TiO_2 hollow sphere. On the other hand, the reverse structure of TiO_2@CdS DHS exhibits a faster degradation rate of RhB than pure CdS hollow spheres at the early stage of the photocatalysis due to the enhanced separation of photo-generated electrons and holes in the CdS/TiO_2 heterojunction. However, when compared these two DHS samples, the CdS@TiO_2 DHS exhibits a much weaker photocatalytic activity than the TiO_2@CdS DHS, though the former has a wider visible-light absorption than the later. Considering their different architecture structures, there are three possible reasons for their different photocatalytic activity. The first reason is that the light harvesting of the CdS inner shell is reduced by the light-scattering of the TiO_2 outer shell in CdS@TiO_2 DHS [29]. As a result, less electron–hole pairs generate in CdS@TiO_2 DHS compared to TiO_2@CdS DHS. The second reason is the presence of hexagonal phase CdS in CdS@TiO_2 DHS. The mixture of cubic and hexagonal CdS nanocrystals shows the lowest photocatalytic activity in comparison with either pure cubic CdS nanocrystals or hexagonal CdS nanocrystals due to the crystalline defects occurring at the interface of the two phases [30]. These crystalline defects can facilitate the recombination of photo-generated electrons and holes. The third reason for the weaker photocatalytic activity of CdS@TiO_2 DHS is ascribe to its relative smaller specific surface area.

4. Conclusions

TiO_2@CdS and CdS@TiO_2 DHS have been successfully synthesized by a template method, and their morphology, crystal structure, optical property and visible-light photocatalytic properties were studied. The DHS structure is 540 nm in diameter and consists of 20 nm CdS layer and 50 nm TiO_2 layer. The absorption edges of TiO_2@CdS and CdS@TiO_2 DHS are around 515 nm and 540 nm, and the corresponding bandgap are 2.4 eV and 2.3 eV, respectively. The experiments of photocatalytic degradation of RhB indicated that coupling TiO_2 hollow spheres with CdS can enhance the photocatalytic properties of TiO_2 hollow spheres and TiO_2@CdS DHS exhibits better photocatalytic properties than CdS@TiO2.

Acknowledgments

This work was supported by the Natural Science Foundation of China (Nos. 60806045, 11074220, 51172208 and 51072182), National Basic Research Program of China (973 Program) (No. 2010CB933501), Zhejiang Provincial Natural Science Foundation of China (Nos. Y4100310, Y1110519).

References

[1] J.Q. Li, D.F. Wang, H. Liu, Z.L. He, Z.F. Zhu, Appl. Surf. Sci. 257 (2011) 5879.
[2] J. Lin, J.C. Yu, J. Photochem. Photobiol. A 116 (1998) 63.
[3] W. Ho, J.C. Yu, J. Mol. Catal. A 247 (2006) 268.
[4] L. Wu, J.C. Yu, X.Z. Fu, J. Mol. Catal. A 244 (2006) 25.
[5] C.L. Yu, D.J. Cai, K. Yang, J.C. Yu, Y. Zhou, C.F. Fan, J. Phys. Chem. Solids 71 (2010) 1337.
[6] K. Drew, G. Girishkumar, K. Vinodgopal, P.V. Kamat, J. Phys. Chem. B 109 (2005) 11851.
[7] S. In, A. Orlov, R. Berg, F. Garc, S. Pedrosa-Jimenez, M.S. Tikhov, D.S. Wright, R.M. Lambert, J. Am. Chem. Soc. 129 (2007) 13790.
[8] J.H. Park, S. Kim, A.J. Bard, Nano Lett. 6 (2006) 24.
[9] M. Sathish, B. Viswanathan, R.P. Viswanath, C.S. Gopinath, Chem. Mater. 17 (2005) 6349.
[10] T. Tatsuma, S. Saitoh, P. Ngaotrakanwiwat, Y. Ohko, A. Fujishima, Langmuir 18 (2002) 7777.
[11] J.Y. Wang, Z.H. Liu, Q. Zheng, Z.K. He, R.X. Cai, Nanotechnology 17 (2006) 4561.

[12] C.H. Li, F. Wang, J. Zhu, J.C. Yu, Appl. Catal. B: Environ. 100 (2010) 433.
[13] S.L. Bai, H.Y. Li, Y.J. Guan, S.T. Jiang, Appl. Surf. Sci. 257 (2011) 6406.
[14] C.Y. Su, C.L. Shao, Y.C. Liu, J. Colloid Interface Sci. 359 (2011) 220.
[15] S.C. Hayden, N.K. Allam, M.A. El-Sayed, J. Am. Chem. Soc. 132 (2010) 14406.
[16] A.H. Zyoud, N. Zaatar, I. Saadeddin, C. Ali, D. Park, G. Campet, H.S. Hilal, J. Hazard. Mater. 173 (2010) 318.
[17] J.G. Yu, S.W. Liu, H.G. Yu, J. Catal. 249 (2007) 59.
[18] X.F. Song, L. Gao, J. Phys. Chem. C 111 (2007) 8180.
[19] Y.Z. Jiao, C.X. Peng, F.F. Guo, Z.H. Bao, J.H. Yang, L. Schmidt-Mende, R. Dunbar, Y. Qin, Z.F. Deng, J. Phys. Chem. C 115 (2011) 6405.
[20] H. Zhang, X. Zhang, X.L. Yang, J. Colloid Interface Sci. 348 (2010) 431.
[21] J.G. Yu, H.T. Guo, S.A. Davis, S. Mann, Adv. Funct. Mater. 16 (2006) 2035.
[22] C.X. Song, D.B. Wang, Y.H. Xu, Z.S. Hu, Mater. Lett. 65 (2011) 908.
[23] Y. Kondo, H. Yoshikawa, K. Awaga, M. Murayama, T. Mori, K. Sunada, S. Bandow, S. Iijima, Langmuir 24 (2008) 547.
[24] H.Q. Wang, M. Miyauchi, Y. Ishikawa, A. Pyatenko, N. Koshizaki, Y. Li, L. Li, X.Y. Li, Y. Bando, D. Golberg, J. Am. Chem. Soc. 133 (2011) 19102.
[25] M. Nakamura, K. Ishimura, Langmuir 24 (2008) 5099.
[26] X.F. Song, L. Gao, Langmuir 23 (2007) 11850.
[27] D.P. Wang, H.C. Zeng, Chem. Mater. 21 (2009) 4811.
[28] N. Serpone, P. Maruthamuthu, P. Pichat, E. Pelizzetti, H. Hidaka, J. Photochem. Photobiol. A: Chem. 85 (1995) 247.
[29] X. Wu, G.Q. Lu, L.Z. Wang, Energy Environ. Sci. 4 (2011) 3565.
[30] N.Z. Bao, L.M. Shen, T. Takata, K. Domen, A. Gupta, K. Yanagisawa, C.A. Grimes, J. Phys. Chem. C 111 (2007) 17527.